

# DAMAGE AND MECHANICAL REPAIR OF COMPOSITE LAMINATES: EFFECTS OF EMBEDDED DEFECTS AND LOW-VELOCITY IMPACTS

Guijia Zhang<sup>1</sup>, Mingbo Tong<sup>1</sup>, Bing Yan<sup>2</sup>, Fangli Wang<sup>3</sup>, Henghui Zhang<sup>1</sup>

<sup>,1</sup>Nanjing University of Aeronautics and Astronautics, Nanjing 210016, China

<sup>2</sup> Chinese Aeronautical establishment, Beijing, China

<sup>3</sup> College of Mechanical and Electrical Engineering, Jinling Institute of Technology, Nanjing, China

#### **Abstract**

Both numerical simulations and experimental methods were employed to investigate the compressive strength of laminates with pre-embedded defects and under low-velocity impact. The CAI of laminates with embedded defects was also examined. Bolted repairs were implemented around the damaged area to investigate the effectiveness of improving compressive strength for both scenarios. The results obtained from the numerical simulation and the experimental results were combined to analyze the damage modes of the laminates with pre-embedded defects and under low velocity impact and mechanical repairs and their effects on the damage development and failure during compression.

Keywords: Laminates; Delamination; CAI; Failure analysis; Low-velocity Impact

#### 1. Introduction

Composite materials are widely used in aircraft structures such as vertical tails, horizontal stabilizers, and fuselage skin panels due to their superior properties[1], [2], [3]. However, carbon fiber-reinforced polymers (CFRPs) in composite laminates are particularly susceptible to delamination during production and service caused by resin bubbles, dropped tools, and foreign object impacts[4], [5], [6], [7], [8]. This damage is visible by the naked eye, called barely visible impact damage (BVID), and hard-to-detect delamination damage poses significant safety hazards to the use of composite structures[9], [10], [11], [12].

Researchers commonly employ compression-after-impact (CAI) tests to assess the effects of low-velocity impact (LVI) on structural performance[13], [14], [15]. It is generally assumed that composite laminates lack initial defects during these evaluations, although delamination damage is an inevitable issue during their use [16], [17], [18], [19]. Assessing the impact of initial delamination damage on LVI and CAI tests on laminates is crucial.

While testing offers realistic failure modes and results, it is time-consuming and costly. The Small sample size used in the test, influenced by the preparation process, leads to highly dispersed results. Simulations are a powerful, cost-effective, and computationally efficient tool for analyzing the LVI and CAI in composite laminates. Modeling methods vary based on research objectives, including separate LVI models[20], [21], [22], [23], [24], CAI models[25], [26], and full-process simulations[27], [28], [29] that combine both. In these models, failure criteria such as the Hashin[30] and Puck[31], [32] criteria simulate damage initiation in each laminate layer[33], [34]. Continuum damage mechanics methods (CDM)[35], [36], [37], [38], [39], commonly used to simulate damage propagation, are prevalent. Delamination damage is a critical concern in LVI simulations. Delamination damage poses an essential problem for LVI simulations, effectively simulated by the Cohesive Zone Model (CZM)[40], [41], [42], [43]. In Abaqus, this modeling uses cohesive elements, surfaces, or contacts.

This study employed numerical simulations and experimental methods to investigate the LVI and CAI tests of laminates with and without pre-embedded defects (delamination damage). The study

compared the performance of three common laminate layups used in aircraft fuselage panels under both scenarios. Additionally, it explored how the depth of delamination affects the compressive strength of the laminates. The study also examined the compressive strength of laminates with embedded defects after experiencing LVI. Corresponding test pieces for laminates with preembedded defects were created, and bolted repairs were applied to explore the effectiveness of mechanical maintenance in enhancing compressive strength. The efficiency of mechanical repairs was also assessed for laminates under conditions of pre-embedded defects and LVI.

# 2. Specimens and test set-up

## 2.1 Experimental procedure

Specimens were made from 0.13mm unidirectional composite prepreg lamina and 0.3mm woven fabrics chosen to enhance impact resistance. These materials were arranged in three typical laminate layups used in aircraft fuselage panels (refer to Table 1). The dimensions of the test specimens were 150mm×100mm, conforming to the ASTM D7137 standard. The typical dimensions and the location of pre-embedded defects in the specimens are illustrated in Figure 1, where the blue dashed line indicates the location of the pre-embedded defects damage.

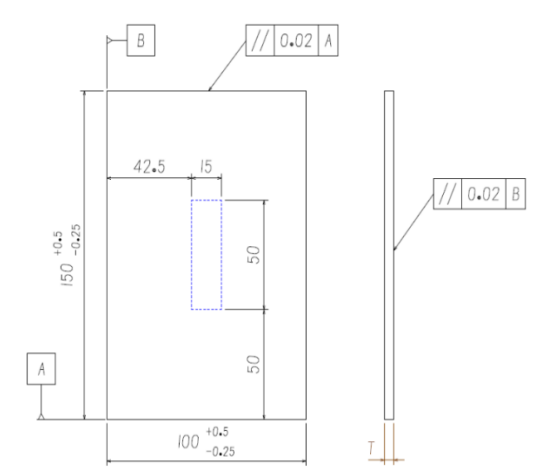


Figure 1. Dimensions of the specimens
Table 1 Type of layup forms

Serial number	Layup forms	Thickness/ mm
А	(45)/(45)/90/45/0/45/90/-45/90/-45/0/90/90/0/-45/90/- 45/90/45/0/45/90/(45)/(45)/(45)/0/0/90/0/0/90/0/(45)	5.44
В	(45)/(45)/45/0/90/-45/0/90/0/-45/90/0/45 /(45)(45)/(45)/0/90/0/90/0/0/(45)	4.27
С	(45)/(45)/90/45/0/45/90/-45/90/-45/0/90/90/0/-45 /90/- 45/90/45/0/45/90/(45)/(45)	3.8

# () represents for the woven fabrics

In line with the research objectives, 16 sets of experiments were conducted, consisting of 96 compression strength tests on typical composite laminates. The specimens were divided into three types: 1) undamaged (18 specimens), 2) with pre-embedded defects (30 specimens), and 3) subjected to low-velocity impact (48 specimens).

In the pre-embedded defects group, the influence of delamination damage on the compressive strength of the test pieces was compared under three different pre-embedded defect positions (in the thickness direction). The layup forms of the test pieces were selected from three typical layup forms of the fuselage skin panels. The configurations of these test specimens are detailed in Table 2.

Table 2 The configurations of test specimens.

Serial Number	Layup Configuration	Pre-embedded Defect Position	Impact damage	Number of Specimens
A-0-N	Α	-	N	6
A-0-Y	Α	-	Y(BVID)	6
A-I-N	Α	1	N	6
A-II-N	Α	II	N	6
A-III-N	Α	III	N	6
B-0-N	В	-	N	6
B-0-Y	В	-	Y(BVID)	6
B-I-N	В		N	6
B-III-N	В	III	N	6
C-0-N	С	-	N	6
C-0-Y	С	-	Y(BVID)	6
C-I-N	С		N	6
C-II-N	С	II	N	6
C-I-Y	С		Y(BVID)	6
C-II-Y	С		Y(BVID)	6
C-II°-N	С	II(Without Repair)	N	6
Total				96

Note: A, B, C represent the three typical layup forms; I, II, III represent the three different preembedded defect locations in Figure 1; Y and N indicate whether the specimen has been subjected to low velocity impact, with Y representing barely visible impact damage (BVID).

For specimens with pre-embedded delamination damage, Hi-Lok bolts are used near the damaged area to enhance compressive strength. The installation positions of the Hi-Lok bolts are illustrated in Figure 2.

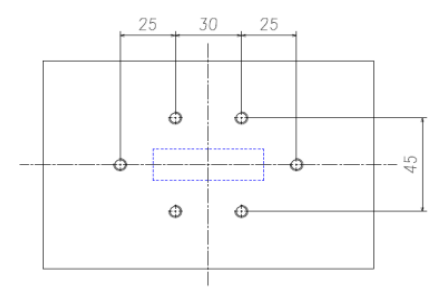


Figure 2 Positions of the Hi-Lok bolts

The locations of the pre-embedded defects are depicted in Figure 3, where 'T' represents the total thickness of the specimen. The defects are prepared from Polytetrafluoroethylene (PTFE). Positions I, II, and III in Table 2 correspond to H=1/3T, H=1/2T, and the junction surface of the longitudinal girder and skin, respectively.

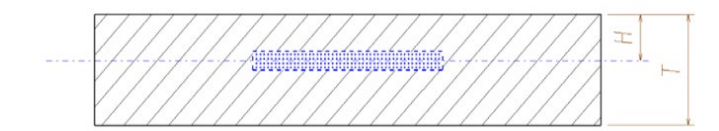


Figure 3 Pre-embedded Delamination Damage Location

## 2.2 LVI tests

LVI experiments were conducted according to the ASTM D7136/D7136M standard using a CLC-A drop weight impact testing machine (see Figure 4.a). The specimen was placed on a base with a 125 mm × 75 mm cut-out and secured by four rubber-tipped clamps, as shown in Figure 4.b. Damage was introduced by an out-of-plane concentrated impact perpendicular to the laminate plane, using a hemispherical impactor. Following the test standard, a 16 mm radius hemispherical impactor made of aluminum was selected, with an impact energy of 6.7 J/mm and a total impact energy of 36 J.

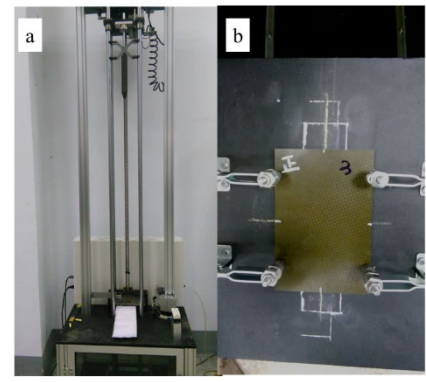


Figure 4 a) CLC-A drop weight impact testing machine b) Support fixture

Before compression testing, specimens with pre-embedded defects were examined using a UPK-T36 ultrasonic immersion C-scan system (see Figure 5). This non-destructive test determined the size and location of the defects (Figure 6.a), and the results were used to map their positions (Figure 6.b).



Figure 5 UPK-T36 ultrasonic immersion C-scan system

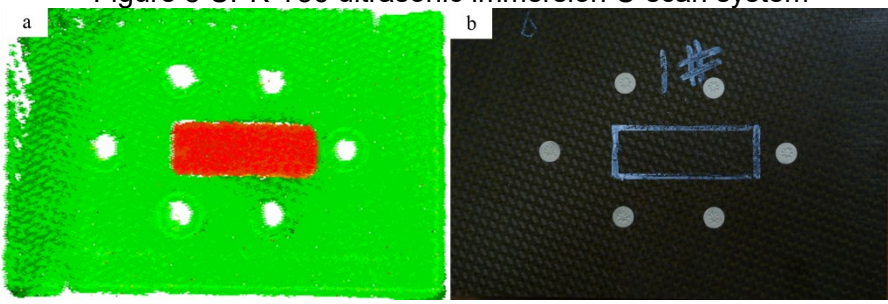


Figure 6 C-scan result for specimens with pre-embedded defects

## 2.3 Compression tests

For compression tests, longitudinal strains were measured at four different positions—two back-to-back on each surface of the specimen—to ensure the application of pure compressive loads and detect any bending or buckling. The compression tests followed the requirements of ASTM D7137 (Figure 7), loading on a WDW-E2000 electronic universal testing machine with displacement loading at a rate of 0.5 mm/min, and strain data was collected every second. For specimens after LVI, the C-scan system was used to measure the inter-laminar damage area.

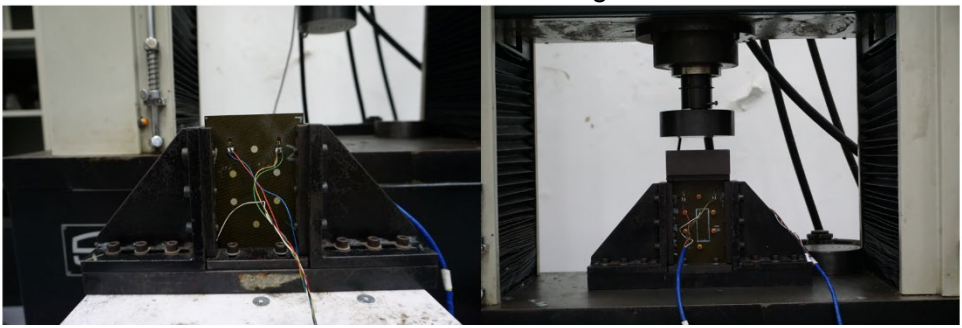


Figure 7 support fixture and strains measured positions

#### 3. Numerical simulation

For laminates under low velocity impact, zero-thickness cohesive elements embedded in ABAQUS/Explicit were introduced between the laminates to predict delamination damage. A damage model based on the Puck failure criterion was established to study the complex damage and failure mechanisms. The interlaminar delamination damage and intralaminar damage behavior in the process of impact and compression after impact (CAI) were considered. A predefined field was used to introduce impact damage into the CAI finite element model, achieving a full-process simulation from low velocity impact to CAI. In addition, the Fastener elements were used to simulate the effect of bolt repair in the corresponding model with pre-embedded defects and low velocity impact.

# 3.1 Intralaminar damage

The Puck criterion was implemented in the simulation model to analyze the intralaminar damage evolution of the composite laminates. The Puck criterion posits that the matrix failure of composite material laminates depends on the stresses on the 'potential' fracture plane. This 'potential' fracture plane is any plane parallel to the fiber direction. The stresses on the fracture plane include a normal stress and two shear stresses, as illustrated in Figure 8.

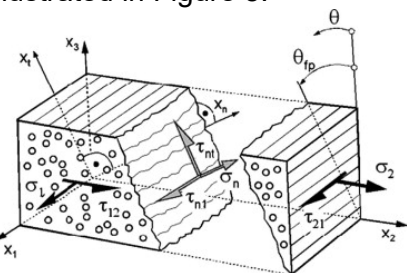


Figure 8 Definition of Stresses Acting on the Fracture Plane

Stresses and strains in the damage principal axis coordinate system can be derived from those in the natural coordinate system through coordinate transformation:

$$\sigma_{n} = \sigma_{2} \cos^{2} \theta + \sigma_{3} \sin^{2} \theta + 2\tau_{23} \sin \theta \cos \theta$$

$$\tau_{nt} = (\sigma_{3} - \sigma_{2}) \sin \theta \cos \theta + \tau_{23} (\cos^{2} \theta - \sin^{2} \theta)$$

$$\tau_{nl} = \tau_{13} \sin \theta + \tau_{12} \cos \theta$$
(1)

Damage in composite materials is categorized into fiber damage (FF) and matrix damage (IFF). The Puck criterion characterizes the material state with a damage parameter (Stress Exposure) to determine whether damage has occurred.

For matrix damage, the damage parameter is expressed as follows:

$$f_{HF}(\theta) = \left[ \left( \frac{1}{R_{\perp}^{t}} - \frac{p_{\perp\psi}^{t}}{R_{\perp\psi}^{A}} \right)^{2} \sigma_{n}^{2}(\theta) + \left( \frac{\tau_{nt}(\theta)}{R_{\perp}^{A}} \right)^{2} + \left( \frac{\tau_{nt}(\theta)}{R_{\perp\parallel}} \right)^{2} \right]^{\frac{1}{2}} + \frac{p_{\perp\psi}^{t}}{R_{\perp\psi}^{A}} \sigma_{n}(\theta) \quad \sigma_{n} \geq 0$$

$$f_{HF}(\theta) = \left[ \left( \frac{p_{\perp\psi}^{c}}{R_{\perp\psi}^{A}} \sigma_{n}(\theta) \right)^{2} + \left( \frac{\tau_{nt}(\theta)}{R_{\perp\parallel}^{A}} \right)^{2} + \left( \frac{\tau_{nt}(\theta)}{R_{\perp\parallel}} \right)^{2} \right]^{\frac{1}{2}} + \frac{p_{\perp\psi}^{c}}{R_{\perp\psi}^{A}} \sigma_{n}(\theta) \quad \sigma_{n} < 0$$

$$\text{Where } R_{\perp}^{A} = \frac{R_{\perp}^{c}}{2(1 + p_{\perp\parallel}^{c})}, \frac{p_{\perp\psi}^{t,c}}{R_{\perp\psi}^{A}} = \frac{p_{\perp\perp}^{t,c}}{R_{\perp\perp}^{A}} \cos^{2}\psi + \frac{p_{\perp\parallel}^{t,c}}{R_{\perp\parallel}^{A}} \sin^{2}\psi, \cos^{2}\psi = \frac{\tau_{nt}^{2}}{\tau_{nt}^{2} + \tau_{nt}^{2}}, \sin^{2}\psi = \frac{\tau_{nt}^{2}}{\tau_{nt}^{2} + \tau_{nt}^{2}}$$

Introducing the slope parameter  $p_{\perp\parallel}^t$ ,  $p_{\perp\perp}^t$ ,  $p_{\perp\parallel}^c$ ,  $p_{\perp\parallel}^c$ , which represents the influence of different normal stress states (tensile and compressive) on the potential fracture plane on the damage.

When determining fiber damage, the transverse Poisson effect is neglected, and the maximum stress criterion is adopted. The fiber failure criterion is as follows:

$$f_{FF}(\theta) = \frac{\sigma_{1}}{R_{\parallel}^{t}} \quad \sigma_{1} \geq \mathbf{0}$$

$$f_{FF}(\theta) = -\frac{\sigma_{1}}{R_{\parallel}^{c}} \quad \sigma_{1} < \mathbf{0}$$
(3)

Most constitutive models for composite materials use two or more tensor-form damage variables to characterize damage. Utilizing the strain equivalence principle, damage state variables define the relationship between the stiffness of damaged and undamaged materials. According to the theory of continuum mechanics, the equivalent stress in the fracture surface coordinate system is defined as[10]:

$$\overset{-h}{\sigma} = M^{h}(\mathbf{D})\sigma^{h} \tag{4}$$

Where  $\mathbf{M}^{r_0}(\mathbf{D})$  is the damage state variable in the fracture surface coordinate system, and its matrix is expressed as:

$$M^{fp}(D) = diag \left[ \frac{1}{1 - d_{f}} \quad \frac{1}{1 - d_{g}} \quad \frac{1}{1 - d_{t}} \quad \frac{1}{1 - d_{gt}} \quad \frac{1}{1 - d_{gt}} \quad \frac{1}{1 - d_{gt}} \right]$$
 (5)

Where  $d_i(i = I, n, t)$  represents the damage variables in three directions under the coordinate system of the matrix fracture surface,  $d_{ij} = 1 - (1 - d_i)(1 - d_j)(i, j = I, n, t, i \neq j)$  is the damage variables corresponding to the shear model.

Establish a damage state variable based on equivalent strain to describe the material, considering the damage evolution law from the onset of loading to complete failure.

$$d_{i}^{k} = \max \left\{ 0, \min \left\{ 1, \frac{\varepsilon_{i}^{k,t}}{\varepsilon_{i}^{k,t} - \varepsilon_{i}^{k,0}} \cdot \left( 1 - \frac{\varepsilon_{i}^{k,0}}{\varepsilon_{i}^{k}} \right) \right\} \right\}$$
 (6)

Where  $\mathbf{k} = \mathbf{t}, \mathbf{c}$ ,  $\varepsilon_i^{\mathbf{k},\mathbf{0}}$  is the strain corresponding to the onset of damage,  $\varepsilon_i^{\mathbf{k},\mathbf{l}}$  is the strain corresponding to material failure,  $\mathbf{c}_c$  is the fracture toughness and  $\mathbf{l}^c$  is characteristic length of each element.

$$\varepsilon_{i}^{k,0} = \sqrt{\langle \varepsilon_{n} \rangle^{2} + \gamma_{nl}^{2} + \gamma_{nt}^{2}}$$

$$\varepsilon_{i}^{k,l} = \frac{2G_{c}}{\sigma_{c}^{0} L^{c}}$$
(7)

## 3.2 Interlaminar damage

To effectively simulate interlaminar delamination damage, zero-thickness cohesive elements, based on a traction-separation constitutive relation, were integrated into the finite element model to represent debonding and delamination.

Camanho[44] and Turon[45] were the first to propose the bilinear constitutive model of the cohesive zone, based on continuum damage mechanics fundamentals. The bilinear constitutive model is the most commonly applied:

$$\begin{cases} \sigma = \mathbf{K}_{\rho} \delta & \delta < \delta^{\mathbf{0}} \\ \sigma = (\mathbf{1} - \mathbf{D}) \mathbf{K}_{\rho} \delta & \delta^{\mathbf{0}} \le \delta < \delta' \\ \sigma = \mathbf{0} & \delta \ge \delta' \end{cases}$$
(8)

Where  $\delta^{\bullet}$  is the relative displacement at the onset of interlaminar damage,  $\delta'$  corresponds to the relative displacement at complete interlaminar failure,  $\delta$  represents the maximum relative displacement occurring during the loading process, D is the damage variable.

A quadratic stress criterion was adopted to ascertain the initiation of interface delamination damage under complex loadings. The quadratic stress failure criterion can be expressed as:

$$\left\{\frac{\langle t_n \rangle}{R_n}\right\}^2 + \left\{\frac{t_s}{R_s}\right\}^2 + \left\{\frac{t_t}{R_t}\right\}^2 = 1 \tag{9}$$

Where  $t_i(i = n, s, t)$  represents the interface stress in the normal direction, first shear direction,

and second shear direction, respectively, and  $R_i(i = n, s, t)$  represents the limit nominal stress in the corresponding direction.

The B-K criterion effectively establishes the relationship between the critical energy release rate and the mixed-mode fracture ratio, and is characterized by its simplicity[46]:

$$\boldsymbol{G}_{\boldsymbol{\kappa}} + (\boldsymbol{G}_{\boldsymbol{\kappa}} - \boldsymbol{G}_{\boldsymbol{\kappa}}) \left( \frac{\boldsymbol{G}_{\boldsymbol{shear}}}{\boldsymbol{G}_{\boldsymbol{\tau}}} \right)^{\eta} = \boldsymbol{G}_{\boldsymbol{\tau}}$$
 (10)

Where  $\eta$  is the exponent in the B-K criterion,  ${\it G}_{\it ic}$  is the critical fracture energy.

## 3.3 Numerical analysis

## 3.3.1 Laminates with pre-embedded defects

In ABAQUS/Standard, a geometric model was created, segmenting the pre-embedded defects and the adjacent laminates into separate parts (Figure 9). For the composite laminates, eight-node reduced-integration solid elements (C3D8R) were employed. Each layer was discretized into a single element in the thickness direction, allowing for detailed observation of each layer's characteristics during failure. To simulate the delaminated defect layer, 0.01mm thick cohesive elements (COH3D8) were used, and the defect layer was connected to adjacent sub-plates using Tie contacts. Surface-to-surface contact constraints were applied to both sub-layers to prevent penetration.

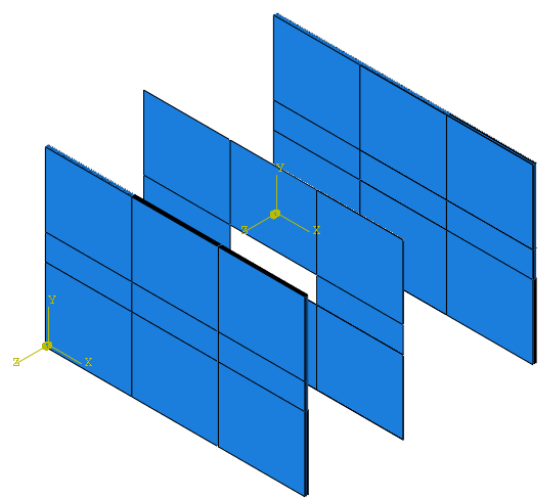


Figure 9 Three parts of the model

Before static loading, an eigenvalue buckling analysis was conducted to determine the node displacement distribution for the first-order buckling mode. These displacements were then used as initial defects in the structure. In the static analysis, 5% of the thickness was used as the initial disturbance. The results of the buckling analysis are displayed in Figure 10.

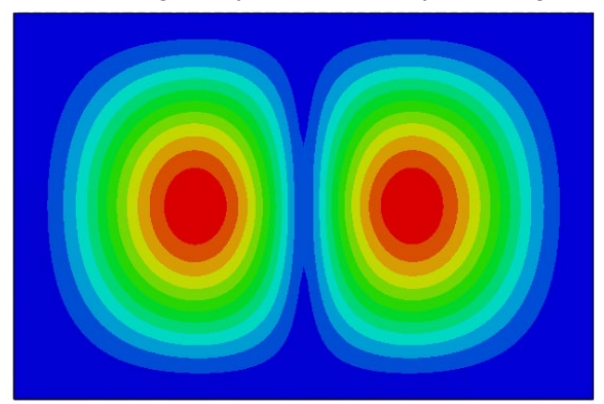


Figure 10 First order buckling model

## 3.3.2 Laminates under LVI

The Abaqus/Explicit solver was employed for the LVI simulation to obtain the impact response and damage modes under impact loads. A 3D finite element model was established, using eight-node reduced-integration solid elements (C3D8R) to simulate the composite material laminates. Each sublayer in the thickness direction was discretized into a single element, with zero-thickness interface elements (COH3D8) inserted between every two layers of different orientation angles. To improve computational efficiency, as illustrated in Figure 11, the mesh near the center was refined, cohesive elements were placed only in this area, while a sparser mesh was used in areas farther from the center. The grid density in the central region was 0.5 mm × 0.5 mm, and the grid density at the outermost edges was 3 mm × 3 mm.

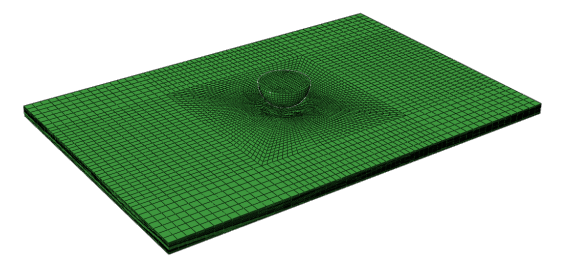


Figure 11 Finite element model of impact

The cohesive elements are set not to be deleted after damage to avoid mutual penetration of the upper and lower sub-layers after delamination. Rigid body constraints were applied to the impactor. Surface-to-surface contact was established between the impactor and the laminate. Hard contact was implemented to replicate typical interaction behavior. Contact forces were calculated using the penalty method. Tangential interactions between contact pairs were modeled using the Coulomb friction model. The friction coefficient was set to 0.3. Fixed support constraints were applied around the laminate. An initial velocity, based on the impact energy, was applied to the impactor.

## 3.3.3 Laminates of CAI

The Abaqus/Explicit module was employed for the quasi-static simulation of CAI, using the same element configuration and mesh as the impact model. The deformed mesh from the LVI result file served as the initial model to get the displacement of impacted elements. Impact damage from the simulation was integrated into the CAI model using predefined fields, simulating the entire progression from LVI to CAI in the composite structure. A fixed support constraint was applied to the node on the fixed end. The loading end node on the right side was constrained in all degrees of freedom except in the direction of the compressive load. Side nodes were constrained to limit displacement along the thickness direction. An equation constraint was set between the reference point and the loading end. Compression displacement load was applied at the reference point, as illustrated in Figure 12.

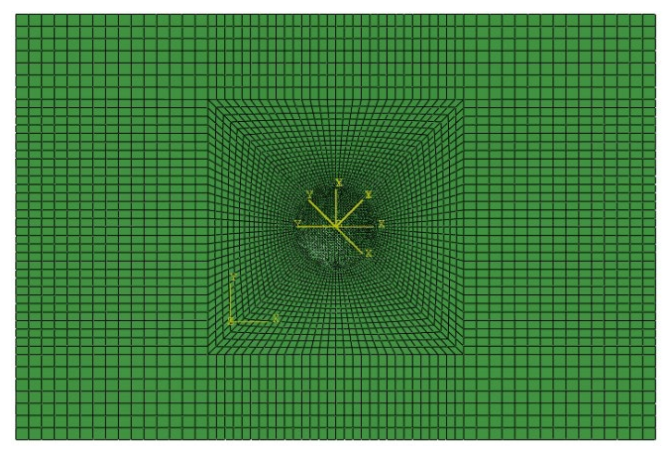


Figure 12 Finite element model of CAI

## 3.3.4 Laminates with bolt repair

The bolts were modeled as solids, and the model was established at the corresponding positions with contacts set (Figure 13).

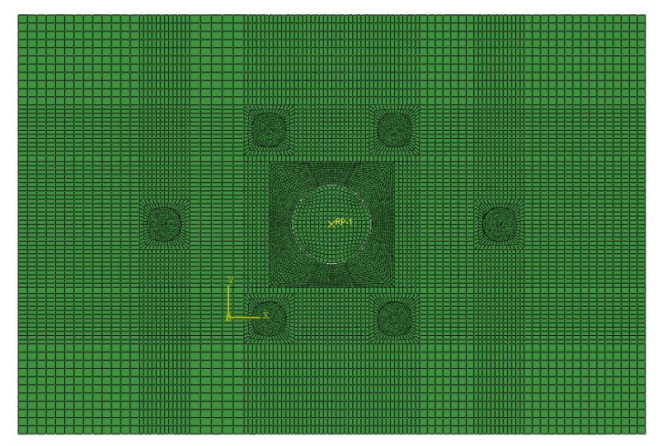


Figure 13 Finite element model with bolt repair

## 4. Results and discussion

# 4.1 Undamaged specimens

Table 3 Compressive strength of undamaged specimens

rabio o compreserve sa engar er anaamagea epecimene				
Serial number	0° unidirectional	Compressive	Relative to A-0-N	
	tape ratio	strength /MPa	ratio	
A-0-N	29.4%	327.8	1	
B-0-N	40.0%	354.5	1.08	
C-0-N	16.7%	310.7	0.88	

The table 3 shows that among the three laminate types, Type B exhibits the highest compressive strength, followed by Type A, with Type C having the lowest. Furthermore, the variations in compressive strength correspond to changes in the 0° unidirectional tape ratio within the laminates.

#### 4.2 LVI and CAI

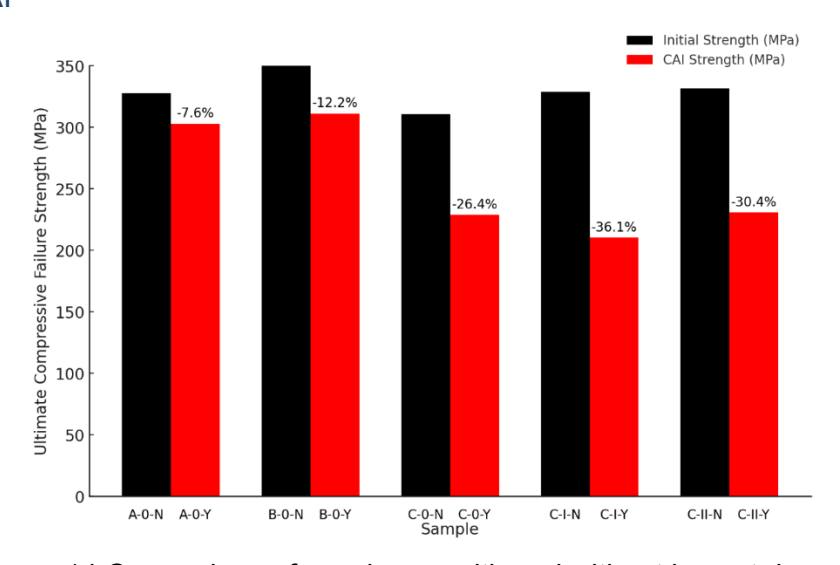


Figure 14 Comparison of specimens with and without impact damage

The Figure 14 shows reductions in compressive strength of some samples after LVI. Different laminates exhibit a strength decrease of 7.6% to 36.1% compared to their undamaged state. Impact damage severity varies by laminate layup type; Type A laminates show the least strength reduction at 7.6%, indicating superior impact resistance. In contrast, Type C laminates suffer more severe reductions, with decreases exceeding 26%. Additionally, laminates with pre-embedded damage show further reduced resistance, especially Type I samples, which exhibit the most significant decline in compressive strength.

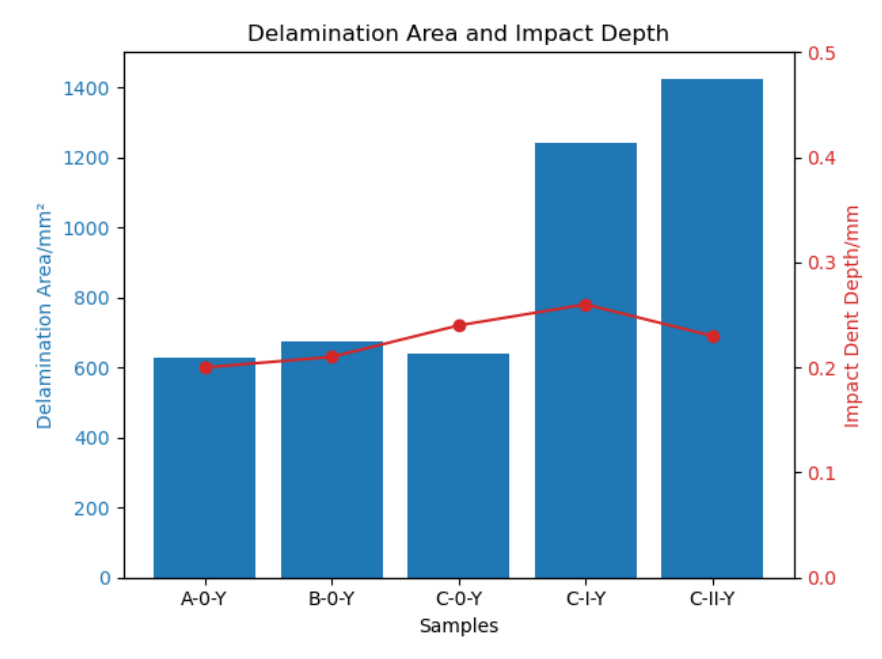


Figure 15 Damaged area and impact dent depth

After impact, the damaged area and impact dent depth for each group of test specimens were measured (Figure 15). For the C-I-Y and C-II-Y groups, the damaged area encompassed both preembedded defects and impact damage, including overlaps between them. Only the total projected area was measured. The analysis of the samples A, B, and C, which vary in thickness and lamination patterns, reveals a clear correlation between thickness and impact resistance, with thicker samples generally offering better protection against impacts. Sample A, the thickest, showed the lowest impact dent depth, confirming that increased thickness enhances a material's ability to absorb and distribute impact energy. This underscores the importance of considering both material thickness and lamination strategies in designing materials for enhanced impact resistance.

As for the simulation of LVI, take the results of group C-0-Y as an example. The contact force-time curve obtained between the laminate and the impactor was output to study the change in impactor force during the impact process (Figure 16). The figure shows that the contact time during the impact was very short, and the impact force changed drastically. The process can be mainly divided into three stages: (1) Undamaged stage: Initially, there was no contact between the impactor and the laminate, resulting in zero contact force. This stage was extremely brief, followed by a rapid increase in contact force with significant fluctuations; (2) Damage evolution stage: The laminate was bent under the impact, initiating matrix cracking and subsequent interlayer delamination. Contact force fluctuated violently, particularly near its peak value. At t=0.018s, the contact force peaked at 10.08kN, coinciding with the impactor speed dropping to zero; (3) Impactor rebound stage: Following damage, the laminate's stiffness and load-bearing capacity decreased, causing the impactor to rebound and the contact force to gradually decrease to zero. The three areas marked 1, 2, and 3 in the figure correspond to the stages of matrix damage in the laminate, delamination between layers, and impactor rebound, respectively. The first wave represents the initiation of matrix damage; the second wave signals the initiation and evolution of delamination; the third wave indicates laminate rebound while internal damage continues to expand. The figure also shows that during the loading and unloading stages, the contact force during unloading is significantly less than during loading, due primarily to decreased stiffness and load-bearing capacity of the laminate after impact. Irrecoverable indentations form on the laminate surface after impact. The area within the load-displacement curve represents the energy absorbed by the laminate during the impact.

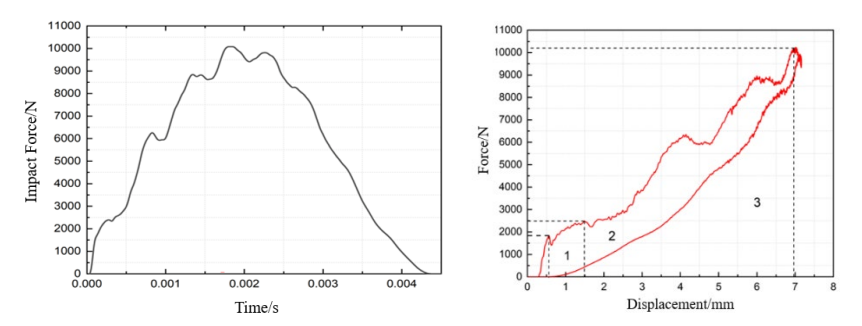


Figure 16 impact force-time and displacement curves

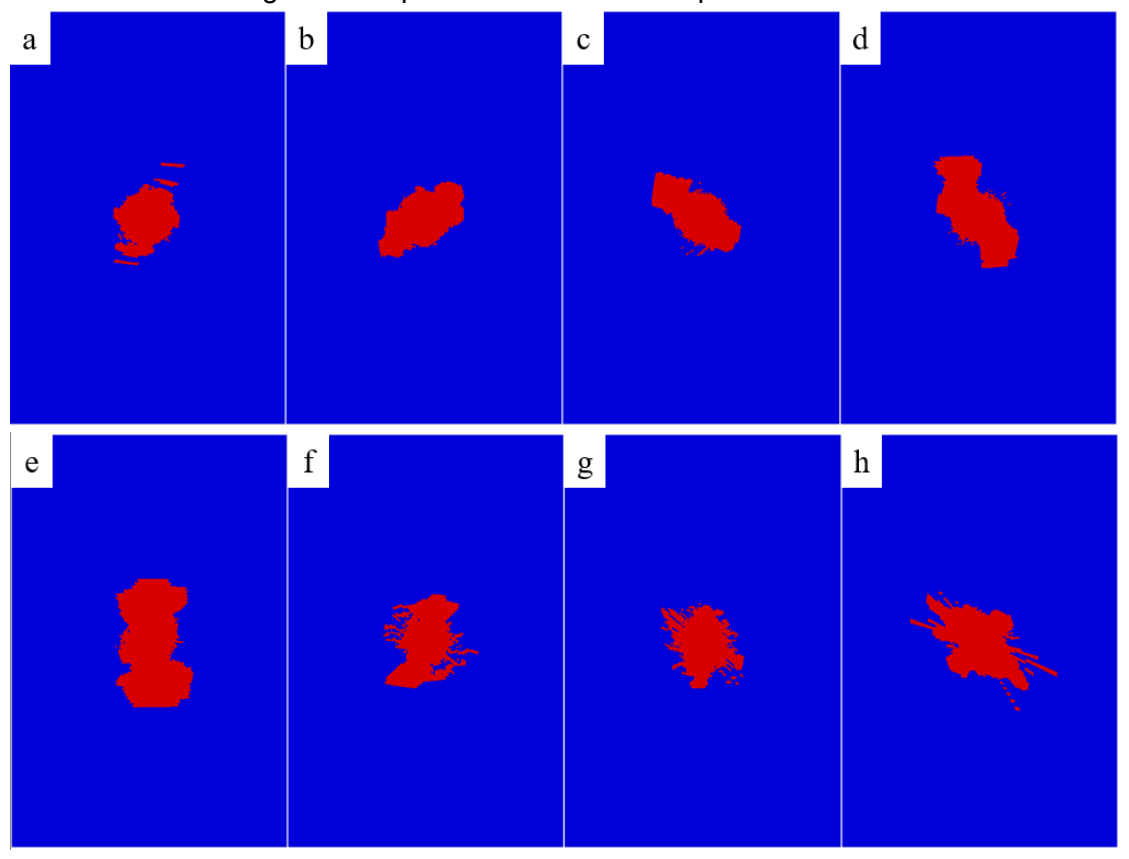


Figure 17 Matrix damage for certain sub-layers (a) layer 4 (b) layer 6 (c) layer 8 (d) layer 10 (e) layer 13 (f) layer 16 (g) layer 18 (h) layer 22

At an impact energy of 36J, the composite laminate primarily sustained matrix damage and interlayer delamination. Fiber breakage was noted in some sub-layers, without any fiber extrusion damage. Damage for certain sub-layers and interface layers under this impact energy are depicted in Figure 17. In these diagrams, red indicates the damage of the element. In sub-layer matrix damage, the first lamination angle represents this sub-layer's ply angle, and the second angle corresponds to the ply angle of the sub-layer below it. As shown in Figure 17, the sub-layer distant from the impact point experiences high tensile stress from impact bending deformation, resulting in extensive matrix cracking damage. Initially, matrix cracking follows the fiber direction of the sub-layer. As delamination progresses, cracking shifts to align with the fiber direction of the sub-layer below, influenced by stress state changes due to delamination. Under LVI, matrix cracking first manifests in the uppermost sub-layer. As the impact load increases, matrix cracking extends to sub-layers distant from the impact point, aligning with the fiber directions of these layers.

The simulated delamination area is 523.5 mm<sup>2</sup>, and the delamination area obtained by ultrasonic C-scan is 533.8 mm<sup>2</sup>, with an error of 1.93%.



Figure 18 Delamination area of simulation and experiment

Under compressive loading, matrix compression initially extends from the impact point. At peak load, fibers undergo compression failure and propagate through the entire laminate along the load direction. Matrix compression and delamination damages expand, local sub-layers buckle, and the laminate compresses. This damage, observed as halfway through the laminate, matches the test observations shown in Figure 19.

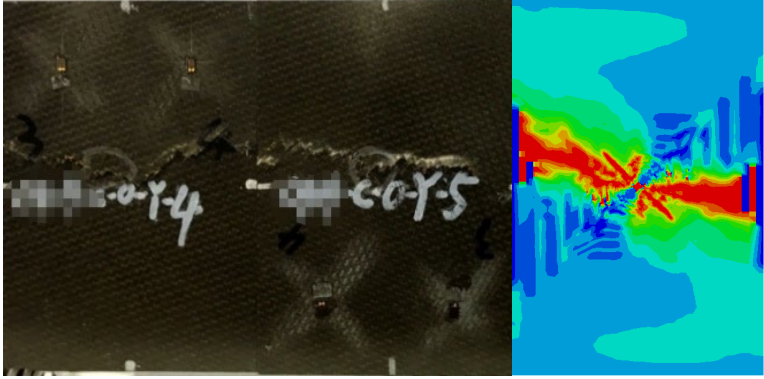


Figure 19 Damage pattern of simulation and experiment

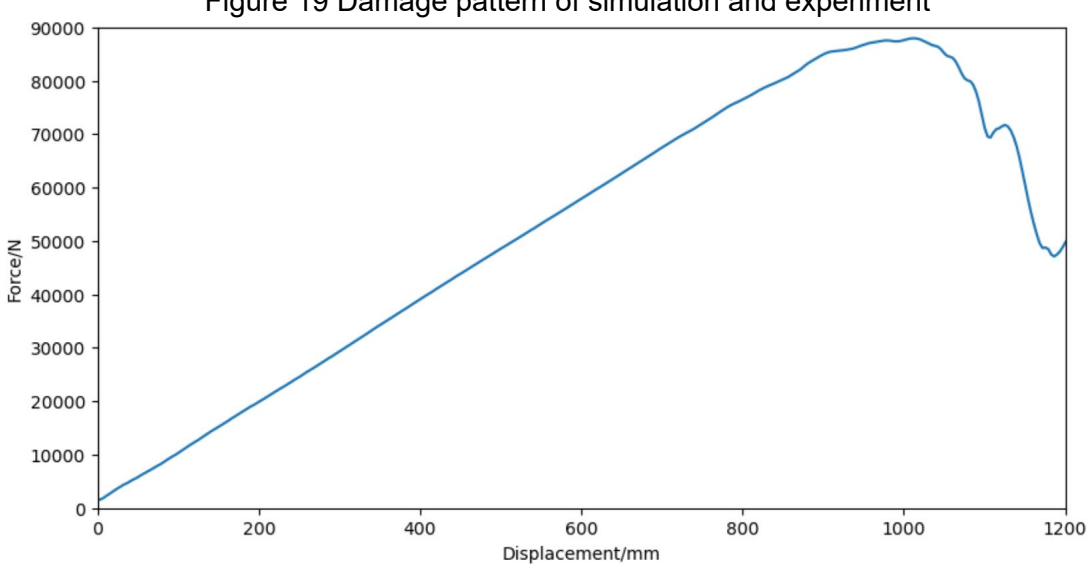


Figure 20 Load-displacement curve of CAI simulation

When damage accumulates to fiber compression failure, energy release causes the load to suddenly drop, a phenomenon known as "sudden death" consistent with experimental observations (Figure 20). The prediction error for CAI strength is only 0.09%. This study utilizes various damage types from LVI finite element analysis as the initial damage in the compression failure model. No artificial assumptions about the laminate's damage state post-impact are made, enabling higher prediction accuracy.

## 4.3 Laminates with pre-embedded defects

Laminates with pre-embedded damage and bolt repairs show an enhancement in compressive strength (Table 4), ranging from 5.8% to 12.2%. The impact of embedded defects on compressive strength varies by location and laminate type: Type A laminates with Class III embedded defects achieve the highest compressive strength after bolt repair. Type B laminates with Class I embedded defects show the greatest strength post-repair. For Type C, laminates repaired with bolts and containing Class II defects exhibit the highest strength.

Table 4 Compressive strength with embedded defects after bolt repair

Туре	Serial number	Compressive strength /MPa	Relative to undamaged laminates ratio
	A-0-N	327.8	-
Α	A-I-N	347.9	6.11%
	A-II-N	356.9	7.80%
	A-III-N	368.0	12.28%
	B-0-N	354.5	-
В	B-I-N	397.5	12.11%
	B-III-N	383.7	8.25%
	C-0-N	310.7	-
С	C-I-N	328.9	5.84%
	C-II-N	331.6	6.69%

To assess the repair effect of bolts on the compression performance of laminates with embedded damage, two experimental control groups, C-II°-N and C-II-N, were established. The two test groups consisted of laminates with type II embedded damage: one group without bolt repair and another with bolt repair. The test results for both groups are presented in the Table 5 below.

Table 5 Comparison of compressive strength in bolt repair control group

Serial number	Compressive strength /MPa	Relative to C-0-N ratio	Relative to C-II°-N ratio
C-0-N	310.7	-	-
C-II°-N	324.6	4.40%	-
C-II-N	331.6	6.69%	2.2%

The compressive strength of both test sets with Type II embedded defects is higher than that of the wall panels without such defects, with or without bolt repairs. For Class C siding with Type II embedded damage, bolt repairs resulted in a 2.2% increase in compressive strength.

#### 5. Conclusion

This paper develops finite element (FE) models for intralaminar damage and interlaminar delamination to predict LVI and CAI behavior with pre-embedded defects and compares them with experimental results

The influence of pre-embedded defects on the compressive strength varies for different positions in types A, B, and C layup forms. The study examined the sensitivity of compressive strength to thickness location and delamination damage area, finding variations in compressive strength at different thickness positions. The strength generally decreases when delamination occurs at one-third or one-quarter of the thickness. The sensitivity of compressive strength to delamination at different thickness levels varies; typically, it decreases with increasing delamination area, but remains relatively unchanged when delamination is at mid-thickness, even with significant damage.

The impact of damage varies for different layup forms. Type A have the best impact resistance, with a 7.6% reduction in CAI strength, while Type C, with the poorest impact resistance, show over a 26% reduction. The impact on laminates with different pre-embedded defects also varies. Comparing C-0-Y, C-I-Y, and C-II-Y test groups, laminates with pre-embedded defects show further decreased impact resistance, with group I pre-embedded defects laminates experiencing the largest reduction in compressive strength. Laminates with pre-embedded damage that after bolt repairs showed an increase in compressive strength, with improvements ranging from 5.8% to 12.2%.

#### 6. Contact Author Email Address

zhangquijia@nuaa.edu.cn

## 7. Copyright Statement

The authors confirm that they, and/or their company or organization, hold copyright on all of the original material included in this paper. The authors also confirm that they have obtained permission, from the copyright holder of any third party material included in this paper, to publish it as part of their paper. The authors confirm that they give permission, or have obtained permission from the copyright holder of this paper, for the publication and distribution of this paper as part of the ICAS proceedings or as individual off-prints from the proceedings.

#### References

- [1] P. Shyprykevich, "Damage Tolerance of Composite Aircraft Structures: Analysis and Certification," 1997.
- [2] H. Dębski and M. Ostapiuk, "Numerical FEM analysis for the part of composite helicopter rotor blade," *J. KONES Powertrain Transp.*, vol. 19, pp. 70–77, Jan. 2015, doi: 10.5604/12314005.1137313.
- [3] A. Gliszczynski, "Numerical and experimental investigations of the low velocity impact in GFRP plates," *Compos. Part B Eng.*, vol. 138, pp. 181–193, Apr. 2018, doi: 10.1016/j.compositesb.2017.11.039.
- [4] P. N. B. Reis, J. A. M. Ferreira, P. Santos, M. O. W. Richardson, and J. B. Santos, "Impact response of Kevlar composites with filled epoxy matrix," *Compos. Struct.*, vol. 94, no. 12, pp. 3520–3528, Dec. 2012, doi: 10.1016/j.compstruct.2012.05.025.
- [5] L. B. Vogelesang and A. Vlot, "Development of fibre metal laminates for advanced aerospace structures," *J. Mater. Process. Technol.*, vol. 103, no. 1, pp. 1–5, Jun. 2000, doi: 10.1016/S0924-0136(00)00411-8.
- [6] Q. Gao, W.-H. Liao, and L. Wang, "On the low-velocity impact responses of auxetic double arrowed honeycomb," *Aerosp. Sci. Technol.*, vol. 98, p. 105698, Mar. 2020, doi: 10.1016/j.ast.2020.105698.
- [7] S. Fakhreddini-Najafabadi, M. Torabi, and F. Taheri-Behrooz, "An experimental investigation on the low-velocity impact performance of the CFRP filled with nanoclay," *Aerosp. Sci. Technol.*, vol. 116, p. 106858, Sep. 2021, doi: 10.1016/j.ast.2021.106858.
- [8] F. L. Yang, Y. Q. Wang, and Y. Liu, "Low-velocity impact response of axially moving functionally graded graphene platelet reinforced metal foam plates," *Aerosp. Sci. Technol.*, vol. 123, p. 107496, Apr. 2022, doi: 10.1016/j.ast.2022.107496.
- [9] C. Soutis and P. T. Curtis, "Prediction of the post-impact compressive strength of cfrp laminated composites," *Compos. Sci. Technol.*, vol. 56, no. 6, pp. 677–684, Jan. 1996, doi: 10.1016/0266-3538(96)00050-4.
- [10] N. Li and P. H. Chen, "Micro-macro FE modeling of damage evolution in laminated composite plates subjected to low velocity impact," *Compos. Struct.*, vol. 147, pp. 111–121, Jul. 2016, doi: 10.1016/j.compstruct.2016.02.063.
- [11] S. N. A. Safri, M. T. H. Sultan, M. Jawaid, and K. Jayakrishna, "Impact behaviour of hybrid composites for structural applications: A review," *Compos. Part B Eng.*, vol. 133, pp. 112–121, Jan. 2018, doi: 10.1016/j.compositesb.2017.09.008.
- [12] B. Yang, Y. Chen, J. Lee, K. Fu, and Y. Li, "In-plane compression response of woven CFRP composite after low-velocity impact: Modelling and experiment," *Thin-Walled Struct.*, vol. 158, p. 107186, Jan. 2021, doi: 10.1016/j.tws.2020.107186.
- [13] D. Ghelli and G. Minak, "Low velocity impact and compression after impact tests on thin carbon/epoxy laminates," *Compos. Part B Eng.*, vol. 42, no. 7, pp. 2067–2079, Oct. 2011, doi: 10.1016/j.compositesb.2011.04.017.
- [14] B. Ostré, C. Bouvet, C. Minot, and J. Aboissière, "Experimental analysis of CFRP laminates subjected to compression after edge impact," *Compos. Struct.*, vol. 152, pp. 767–778, Sep. 2016, doi: 10.1016/j.compstruct.2016.05.068.
- [15] M. A. Caminero, I. García-Moreno, and G. P. Rodríguez, "Experimental study of the influence of thickness and ply-stacking sequence on the compression after impact strength of carbon fibre reinforced epoxy laminates," *Polym. Test.*, vol. 66, pp. 360–370, Apr. 2018, doi: 10.1016/j.polymertesting.2018.02.009.
- [16] S. F. Nikrad, S. Keypoursangsari, H. Asadi, A. H. Akbarzadeh, and Z. T. Chen, "Computational study on compressive instability of composite plates with off-center delaminations," *Comput. Methods Appl. Mech. Eng.*, vol. 310, pp. 429–459, Oct. 2016, doi: 10.1016/j.cma.2016.07.021.
- [17] L. Zhao, Y. Liu, H. Hong, K. Wang, and J. Zhao, "Compressive failure analysis for low length-width ratio composite laminates with embedded delamination," *Compos. Commun.*, vol. 9, pp. 17–21, Sep. 2018, doi: 10.1016/j.coco.2018.04.005.
- [18] Q. Sun *et al.*, "Experimental and computational analysis of failure mechanisms in unidirectional carbon fiber reinforced polymer laminates under longitudinal compression loading," *Compos. Struct.*, vol. 203, pp. 335–348, Nov. 2018, doi: 10.1016/j.compstruct.2018.06.028.
- [19] C. Hu, Y. Bai, Z. Xu, J. Qiu, R. Wang, and X. He, "Progressive damage behavior of composite L-stiffened structures with initial delamination defects under uniaxial compression: Experimental and numerical investigations," *Polym. Compos.*, vol. 43, no. 6, pp. 3765–3781, 2022, doi: 10.1002/pc.26654.
- [20] A. Faggiani and B. G. Falzon, "Predicting low-velocity impact damage on a stiffened composite panel," Compos. Part Appl. Sci. Manuf., vol. 41, no. 6, pp. 737–749, Jun. 2010, doi: 10.1016/j.compositesa.2010.02.005.
- [21] N. Hongkarnjanakul, C. Bouvet, and S. Rivallant, "Validation of low velocity impact modelling on different stacking sequences of CFRP laminates and influence of fibre failure," *Compos. Struct.*, vol. 106, pp. 549–559, Dec. 2013, doi: 10.1016/j.compstruct.2013.07.008.
- [22] S. Long, X. Yao, and X. Zhang, "Delamination prediction in composite laminates under low-velocity impact," *Compos. Struct.*, vol. 132, pp. 290–298, Nov. 2015, doi: 10.1016/j.compstruct.2015.05.037.
- [23] S. Jäger, A. Pickett, and P. Middendorf, "A Discrete Model for Simulation of Composites Plate Impact Including Coupled Intra- and Inter-ply Failure," *Appl. Compos. Mater.*, vol. 23, no. 2, pp. 179–195, Apr. 2016, doi: 10.1007/s10443-015-9455-2.
- [24] M. Schwab and H. E. Pettermann, "Modelling and simulation of damage and failure in large composite

- components subjected to impact loads," *Compos. Struct.*, vol. 158, pp. 208–216, Dec. 2016, doi: 10.1016/j.compstruct.2016.09.041.
- [25] P. Rozylo, H. Debski, and T. Kubiak, "A model of low-velocity impact damage of composite plates subjected to Compression-After-Impact (CAI) testing," *Compos. Struct.*, vol. 181, pp. 158–170, Dec. 2017, doi: 10.1016/j.compstruct.2017.08.097.
- [26] T. Ouyang, R. Bao, W. Sun, Z. Guan, and R. Tan, "A fast and efficient numerical prediction of compression after impact (CAI) strength of composite laminates and structures," *Thin-Walled Struct.*, vol. 148, p. 106588, Mar. 2020, doi: 10.1016/j.tws.2019.106588.
- [27] W. Tan, B. G. Falzon, L. N. S. Chiu, and M. Price, "Predicting low velocity impact damage and Compression-After-Impact (CAI) behaviour of composite laminates," *Compos. Part Appl. Sci. Manuf.*, vol. 71, pp. 212–226, Apr. 2015, doi: 10.1016/j.compositesa.2015.01.025.
- [28] M. R. Abir, T. E. Tay, M. Ridha, and H. P. Lee, "Modelling damage growth in composites subjected to impact and compression after impact," *Compos. Struct.*, vol. 168, pp. 13–25, May 2017, doi: 10.1016/j.compstruct.2017.02.018.
- [29] R. Sachse, A. K. Pickett, and P. Middendorf, "Simulation of impact and residual strength of thick laminate composites," *Compos. Part B Eng.*, vol. 195, p. 108070, Aug. 2020, doi: 10.1016/j.compositesb.2020.108070.
- [30] "A Fatigue Failure Criterion for Fiber Reinforced Materials Z. Hashin, A. Rotem, 1973." Accessed: Jun. 08, 2024. [Online]. Available: https://journals.sagepub.com/doi/abs/10.1177/002199837300700404
- [31] A. Puck and H. Schürmann, "FAILURE ANALYSIS OF FRP LAMINATES BY MEANS OF PHYSICALLY BASED PHENOMENOLOGICAL MODELS1," *Compos. Sci. Technol.*, vol. 58, no. 7, pp. 1045–1067, Jul. 1998, doi: 10.1016/S0266-3538(96)00140-6.
- [32] A. Puck and H. Schürmann, "Failure analysis of FRP laminates by means of physically based phenomenological models," *Compos. Sci. Technol.*, vol. 62, no. 12, pp. 1633–1662, Sep. 2002, doi: 10.1016/S0266-3538(01)00208-1.
- [33] P. F. Liu, B. B. Liao, L. Y. Jia, and X. Q. Peng, "Finite element analysis of dynamic progressive failure of carbon fiber composite laminates under low velocity impact," *Compos. Struct.*, vol. 149, pp. 408–422, Aug. 2016, doi: 10.1016/j.compstruct.2016.04.012.
- [34] X. Li et al., "Assessment of failure criteria and damage evolution methods for composite laminates under low-velocity impact," Compos. Struct., vol. 207, pp. 727–739, Jan. 2019, doi: 10.1016/j.compstruct.2018.09.093.
- [35] J. Zhang and X. Zhang, "An efficient approach for predicting low-velocity impact force and damage in composite laminates," *Compos. Struct.*, vol. 130, pp. 85–94, Oct. 2015, doi: 10.1016/j.compstruct.2015.04.023.
- [36] J. Zhou, P. Wen, and S. Wang, "Finite element analysis of a modified progressive damage model for composite laminates under low-velocity impact," *Compos. Struct.*, vol. 225, p. 111113, Oct. 2019, doi: 10.1016/j.compstruct.2019.111113.
- [37] B. Kazemianfar, M. Esmaeeli, and M. R. Nami, "Response of 3D woven composites under low velocity impact with different impactor geometries," *Aerosp. Sci. Technol.*, vol. 102, p. 105849, Jul. 2020, doi: 10.1016/j.ast.2020.105849.
- [38] J. Zhou, B. Liu, and S. Wang, "Finite element analysis on impact response and damage mechanism of composite laminates under single and repeated low-velocity impact," *Aerosp. Sci. Technol.*, vol. 129, p. 107810, Oct. 2022, doi: 10.1016/j.ast.2022.107810.
- [39] J. Jiang, Z. Zhang, J. Fu, H. Wang, and C.-T. Ng, "A newly proposed damage constitutive model for composite laminates under low-velocity impact by considering through-thickness compression damage," *Aerosp. Sci. Technol.*, vol. 137, p. 108267, Jun. 2023, doi: 10.1016/j.ast.2023.108267.
- [40] A. Riccio, A. De Luca, G. Di Felice, and F. Caputo, "Modelling the simulation of impact induced damage onset and evolution in composites," *Compos. Part B Eng.*, vol. 66, pp. 340–347, Nov. 2014, doi: 10.1016/j.compositesb.2014.05.024.
- [41] E. Panettieri, D. Fanteria, and F. Danzi, "A sensitivity study on cohesive elements parameters: Towards their effective use to predict delaminations in low-velocity impacts on composites," *Compos. Struct.*, vol. 137, pp. 130–139, Mar. 2016, doi: 10.1016/j.compstruct.2015.11.011.
- [42] R. Ren, J. Zhong, G. Le, and D. Ma, "Research on intralaminar load reversal damage modeling for predicting composite laminates' low velocity impact responses," *Compos. Struct.*, vol. 220, pp. 481–493, Jul. 2019, doi: 10.1016/j.compstruct.2019.04.012.
- [43] H. Liu *et al.*, "A three-dimensional elastic-plastic damage model for predicting the impact behaviour of fibre-reinforced polymer-matrix composites," *Compos. Part B Eng.*, vol. 201, p. 108389, Nov. 2020, doi: 10.1016/j.compositesb.2020.108389.
- [44] P. P. Camanho, C. G. Davila, and M. F. de Moura, "Numerical Simulation of Mixed-Mode Progressive Delamination in Composite Materials," *J. Compos. Mater.*, vol. 37, no. 16, pp. 1415–1438, Aug. 2003, doi: 10.1177/0021998303034505.
- [45] A. Turon, P. P. Camanho, J. Costa, and C. G. Dávila, "A damage model for the simulation of delamination in advanced composites under variable-mode loading," *Mech. Mater.*, vol. 38, no. 11, pp. 1072–1089, Nov. 2006, doi: 10.1016/j.mechmat.2005.10.003.

